

RESEARCH ARTICLE | OCTOBER 10 2024

Three-dimensional simulations of two-phase plug flow in a microfluidic channel

Santhosh Virappane  ; Reza Azadi  ; Neelarun Mukherjee  ; Peichun Amy Tsai  



Physics of Fluids 36, 102019 (2024)

<https://doi.org/10.1063/5.0220101>



Articles You May Be Interested In

Field-free particle focusing in microfluidic plugs

Biomicrofluidics (April 2012)

Numerical investigation of centrifuge-trapping technique for generating gas–liquid flows in microchannels

Physics of Fluids (August 2022)

An electrokinetic preconcentration trapping pattern in electromembrane microfluidics

Physics of Fluids (September 2022)

Three-dimensional simulations of two-phase plug flow in a microfluidic channel

Cite as: Phys. Fluids **36**, 102019 (2024); doi: [10.1063/5.0220101](https://doi.org/10.1063/5.0220101)

Submitted: 22 May 2024 · Accepted: 12 September 2024 ·

Published Online: 10 October 2024



View Online



Export Citation



CrossMark

Santhosh Virappane, Reza Azadi, Neelarun Mukherjee, and Peichun Amy Tsai

AFFILIATIONS

Department of Mechanical Engineering, University of Alberta, Edmonton, Alberta T6G 1H9, Canada

^aPresent Address: School of Chemistry, The University of Sydney, Sydney, New South Wales 2006, Australia.

^bPresent Address: Department of Earth and Planetary Sciences, The University of Texas at Austin, 23 San Jacinto Blvd., Austin, Texas 78712, USA.

^cAuthor to whom correspondence should be addressed: peichun.amy.tsai@ualberta.ca

ABSTRACT

A fundamental understanding of two-phase flow behavior in microfluidics is crucial for various technological applications across different disciplines, including energy, chemical, and material engineering, as well as biomedical, environmental, and pharmaceutical sciences. In this work, we elucidate the flow fields of low Capillary number [$\text{Ca} \sim O(10^{-3})$] segmented Taylor flows of immiscible CO_2 emulsions/bubbles transported by water in a low aspect ratio microchannel. We conducted high-resolution two- and three-dimensional (2D and 3D) numerical simulations using an improved volume-of-fluid two-phase flow solver and validated their accuracy against experimental data. Our results show that 3D simulations are necessary to accurately capture the dynamics of liquid and supercritical CO_2 emulsions produced at relatively higher Ca . The 3D simulation results also reveal diverse patterns of spanwise vortices, which are overlooked in 2D simulations. Calculating the Q-criterion in 3D revealed that vortices with relatively higher vorticity magnitudes are adjacent to the sidewalls, with the strongest ones emerging across the microchannel in the third dimension. More specifically, gaseous CO_2 bubbles display relatively intense vortex patterns near the interfacial region of the bubble body and the cap due to the influence of the surrounding thin liquid film and slug flow. At higher Ca , liquid and supercritical CO_2 emulsions exhibit similar flow dynamics, however, with prominent vortex patterns occurring in the upstream cap region. These findings pinpoint specific areas within the emulsions/bubbles that require attention to enhance stabilization or exchanging mechanisms for low- Ca Taylor flow of emulsions/bubbles.

Published under an exclusive license by AIP Publishing. <https://doi.org/10.1063/5.0220101>

17 November 2024 17:29:47

I. INTRODUCTION

Emulsion/bubble-based microfluidics, which involves the study and manipulation of two-phase flow regime at the microscopic scale where one phase is dispersed within another continuous phase to form bubbles or emulsions, has attracted significant research effort in the past two decades. This interest is driven by its broad range of applications across different fields, including biomedical research, food processing, material engineering, chemical reactions, and carbon capture and sequestration (CCS) technologies.^{1–3} For example, in biomedical research, emulsions/bubbles generated by microfluidics offer versatile solutions for drug delivery systems, ranging from single emulsions/bubbles to encapsulated forms, enabling precise drug distribution in targeted areas of the body.^{4–6} In the context of CCS, CO_2 storage depends on its interaction with brine within the pores of underground rocks.^{7,8} Multiple mechanisms occurring at microscopic pores, such as capillary, solubility, and mineral trapping, depend on properties of CO_2 including viscosity, surface tension, and its wetting characteristics

with the rocks.^{9,10} Microfluidics can replicate these relevant environments and conditions and provide a useful platform for pore-scale visualization, thereby offering insights into CO_2 emulsion/bubble dynamics and informing strategies to optimize CO_2 sequestration.^{11,12}

Mono-dispersed emulsions/bubbles produced by microfluidics, characterized by stable and uniform-sized production of emulsions or bubbles have attracted much attention.^{5,13,14} Their size and production frequency can be conveniently adjusted by controlling the inlet flow rates¹⁵ using different microfluidic configurations. This adjustability is crucial for precise manipulation and analysis in both research and industrial applications.^{2,16} Emulsions/bubbles in the Taylor slug flow regime are typically produced at low capillary numbers, $\text{Ca} < 0.01$, above which shear stress starts to play a significant role, leading to the formation of smaller, less uniform emulsions/bubbles.¹⁵ Ca is typically defined as $\text{Ca} = \mu_l U_b / \sigma$, where U_b represents the volume-averaged emulsion/bubble velocity, μ_l is the dynamic viscosity of the continuous (carrying) phase, and σ is the interfacial tension between the phases.

Driven by applications, most studies on microfluidic Taylor flow of emulsions/bubbles have examined the dependency of the emulsion/bubble size on control parameters such as channel geometry, flow rates, and fluid properties. For instance, correlations were developed to estimate the size of the produced emulsions/bubbles. Garstecki *et al.*¹⁵ proposed the following scaling law in rectangular T-junction micro-channel under low flow rate input: $L/w = 1 + a(Q_d/Q_c)$. Here, L is the emulsion/bubble length, w is the channel width, a is a constant close to 1, and Q shows the inlet flow rate, with the subscripts “d” and “c” indicating the dispersed and continuous phase, respectively. Other researchers, such as Kovalev *et al.*¹⁷ and Zhao *et al.*,¹⁸ focused on providing comprehensive mapping of the existence domain for Taylor emulsions or bubbles, depending on the properties of the dispersed and continuous phases.

In the past decade, research focus has gradually shifted toward investigating the local flow field in Taylor flow emulsions, particularly using experiments, to understand the underlying physical mechanisms for enhancing mixing, heat, and mass transfer.^{19–21} This exploration has mainly relied on experimental techniques such as micro-particle image velocimetry (μ PIV) and particle tracking velocimetry (μ PTV).^{22–25} For instance, Oishi *et al.*²³ used different fluorescent tracing particles to perform spatial scans over multiple 2D planes of the emulsion and surrounding liquid slug. This approach enabled the first visualization of internal and surrounding flows, revealing the presence of various vortical structures in the emulsion and the surrounding slug.

Experimentally, Azadi *et al.*²⁵ developed a 2D tessellation algorithm to analyze instantaneous near-interface dynamics with PTV data. This approach resolved the normal and tangential velocity components of a deforming bubble adjacent at two-phase interfaces, crucial in assessing the interfacial slip for Taylor bubbles. Liu *et al.*²⁶ highlighted the dependency of the vortex patterns in microfluidic emulsions on Ca, identifying two threshold values that delineate different flow patterns inside the emulsions. They noted that these thresholds values increase with increasing viscosity ratio between the continuous and dispersed phases. However, experimental approaches, while valuable, encounter inherent limitations. For instance, current PIV and PTV methods lack the capability to analyze flow within moving gaseous bubbles, being limited to liquid flow analysis.²⁷ Therefore, developing numerical models that can accurately simulate high-resolution, micron-sized emulsions/bubbles is essential to complement experimental studies.

Numerical simulations on microfluidic Taylor emulsions/bubbles have primarily focused on the breakup process^{28,29} or the effect of flow properties, such as the contact angle and viscosity ratio, on the production of the Taylor emulsion/bubble.^{28,30} Historically, the application of computational fluid dynamics in microfluidics, along with the high computational costs associated with it, has led to a focus on phenomenological flow regimes and the use of 2D domain in studies of micro Taylor flow emulsions/bubbles. In recent years, 2D CFD simulations have shifted to investigate the local flow dynamics within Taylor emulsions.^{31,32} Despite significant advancements in numerical flow solvers and high-performance computing capabilities, the study of 3D flow patterns in microfluidic Taylor emulsion/bubble flow remains a challenge and has been rarely conducted.^{21,29,33–35} Moreover, recent 3D numerical studies have focused on partial aspects of the local flow dynamics in Taylor train emulsions, such as drop breakup processes,³⁵ surrounding flow analysis,³³ or limited 2D plane representations of emulsion flow velocity.²¹

The current literature on emulsion/bubble dynamics significantly is short of comprehensive 3D flow fields of velocity and vorticity evolving in both time and space within the emulsions/bubbles. Such quantitative data are not only crucial for providing deeper insights into the emulsion/bubble dynamics but also for helping industries to enhance the stabilization, mixing, and production of Taylor emulsions/bubbles in microchannels. Comprehensive analyses of velocity and vorticity on various slices help pinpoint areas of intensive flows, which are crucial for effective mixing, dispersion, and heat and mass transfer applications.

In this work, we first quantitatively assess the limitations of 2D numerical models in capturing the flow dynamics of microfluidic Taylor emulsions/bubbles compared to their 3D counterparts. There remains a gap in the literature for quantitative comparisons that highlight this limitation, indicating an area where further research is needed to substantiate the differences and limitations of 2D vs 3D simulation approaches in representing complex fluid dynamics in microfluidic systems. Subsequently, we examine the 3D internal flow dynamics of microfluidic CO₂ emulsions/bubbles in gaseous, liquid, and supercritical (SC) states using high-resolution numerical simulations.

Our 3D results elucidate the flow fields and stability of bubbles and emulsions, which are crucial for several practical applications. For example, understanding the dynamics within CO₂ bubbles and emulsions could enhance the conversion efficiency of CO₂ into valuable chemicals.^{36,37} Furthermore, insights into the flow fields of CO₂ emulsions might enhance CO₂ delivery in greenhouse settings, thereby boosting plant growth and other agricultural operations.³⁸ Additionally, exploring the flow fields in the supercritical (SC) state of CO₂ could shed light on the mechanisms of microscopic trapping within deep saline aquifers, a critical aspect of carbon capture and storage (CCS) applications.¹¹

II. NUMERICAL SIMULATION

A. Problem statement

We conducted computational numerical simulations of CO₂-in-water (Taylor slug) emulsions/bubbles² in a microfluidic T-junction geometry under different pressure conditions. Figure 1 shows the computational domain, comprising a primary microchannel of length L , height l , and width W . This microchannel has a low aspect ratio (AR = 0.33) and a small width of $W = 30 \mu\text{m}$. Water continuously

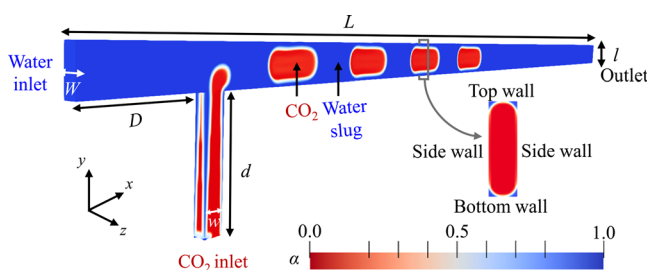


FIG. 1. Schematic representation of the 3D numerical simulation setup of micro-scale bubbles or emulsions of CO₂-in-water produced by a microfluidic T-junction. Water is injected into the main microchannel from an inlet of length L in \hat{x} , width l in \hat{y} , and depth W in \hat{z} . CO₂ is injected from a side microchannel inlet of length d in \hat{y} , width w in \hat{x} , and depth W in \hat{z} . Uniform velocity values are enforced at the inlets; no-slip conditions are applied to the walls; and the outlet is kept at a constant pressure. For 2D simulations, the front and back walls do not exist. Here, α denotes the volume fraction of water.

TABLE I. Thermophysical properties of CO₂ emulsions/bubbles and carrying water utilized for the simulations. SC stands for supercritical. Here, ρ , ν , and σ represent the density, kinematic viscosity (for the specified phases: water and CO₂), and the interfacial tension coefficient between the two phases, respectively.

Pressure (MPa)	ρ_{CO_2} (kg m ⁻³)	$\nu_{\text{CO}_2} \times 10^{-8}$ (m ² s ⁻¹)	$\rho_{\text{H}_2\text{O}}$ (kg m ⁻³)	$\nu_{\text{H}_2\text{O}} \times 10^{-8}$ (m ² s ⁻¹)	σ (mN m ⁻¹)
0.25	4.7	318	997.4	91.6	73.4
1.45	28.2	53.4	997.9	91.5	65.6
3.45	77.2	20.2	998.9	91.4	52.4
5.45	156.5	11	999.7	91.3	41.3
6.45	737.5	10.4	1000.2	91.2	36
7.5	777	8.2	1000.7	91.1	30
8.5	800.8	8.8	1001.1	91.1	30
9.5	819.2	9.1	1001.5	91	25
8.5 (SC)	617.6	7.5	997.8	72.3	30
9.5 (SC)	694	8	998.2	72.3	25

enters the channel at a cross section of $l \times W$, while simultaneously the dispersed phase (CO₂) enters from a side channel of height d , length w , and width W .

The simulations were performed assuming laminar incompressible flow under isothermal conditions, with the two phases considered immiscible. We utilized the interFoam solver from OpenFOAM³⁹ and a modified version, interGCFoam, developed by Maes and Menke,⁴⁰ to accurately model the flow dynamics and interactions between the phases. The physical properties of CO₂ and water, which vary with temperature and pressure, are listed in Table I.

B. Governing equations

One set of Navier–Stokes (NS) equations, derived from the continuity and momentum principles, was solved for the two-phase flow conditions considered in this study. Under the assumptions made, the NS equations are expressed as

$$\vec{\nabla} \cdot \vec{U} = 0, \quad (1)$$

$$\rho(\partial_t \vec{U} + \vec{U} \cdot \nabla \vec{U}) = -\vec{\nabla} p + 2\vec{\nabla} \cdot (\mu \mathbf{D}) + \rho \vec{g} + \vec{f}_\sigma. \quad (2)$$

Here, \vec{U} and p are the velocity and pressure fields, respectively. The strain rate tensor is defined as $\mathbf{D} = (\nabla \vec{U} + (\nabla \vec{U})^T)/2$. The thermophysical properties of the mixture are defined as linear combinations of each phase's properties based on the volume fraction field of the continuous phase, α . α is unity in the continuous phase (denoted by subscript “c”), zero for the dispersed phase (with subscript “d”), and is $0 < \alpha < 1$ over the interface. The density of the mixture is calculated as $\rho = \alpha \rho_c + (1 - \alpha) \rho_d$, and the dynamic viscosity as $\mu = \alpha \mu_c + (1 - \alpha) \mu_d$. In our study, water is the continuous phase, and CO₂ is the dispersed phase. The gravitational force vector is denoted by \vec{g} , and $\vec{f}_\sigma = \sigma \kappa \vec{\nabla} \alpha$ is the interfacial force between the phases. σ is the interfacial tension and assumed to be constant. Based on the continuum surface force (CSF) model by Brackbill *et al.*,⁴¹ the interfacial curvature is defined as $\kappa = -\vec{\nabla} \cdot \vec{n}$, where $\vec{n} = -\vec{\nabla} \alpha / |\vec{\nabla} \alpha|$ is the local interface normal vector.

A transport equation was used to capture the temporal evolution of the interface using the volume of fluid (VOF) method,

$$\partial_t \alpha + \vec{\nabla} \cdot (\vec{U} \alpha) + \vec{\nabla} \cdot [\alpha(1 - \alpha) \vec{U}_r] = 0, \quad (3)$$

where \vec{U}_r is the relative velocity between the phases on the interface, defined as

$$\vec{U}_r = \min[C_\alpha |\vec{U}|, \max(|\vec{U}|)] \vec{n}. \quad (4)$$

Depending on the problem studied, this term can be calibrated by modifying the C_α value to adjust the interface thickness and control the numerical diffusion of the solution.⁴² Hoang *et al.*⁴³ showed that $C_\alpha = 1$ is the optimal value to minimize the numerical diffusion for Taylor flow in a rectangular T-junction. Hence, we used $C_\alpha = 1$ in our simulations.

For low Ca flows, where interfacial tension force is dominant, the definition of κ based on α gradients may cause spurious velocity currents.^{41,44} To mitigate the production of aberrant velocities that could falsify the flow field dynamics in 3D, we used the interGCFoam solver for results provided in Sec. IV B. Unlike interFoam, the α value in each interface cell is smoothed using the following:

$$\alpha_s = C_s \left[[\alpha]_{c \rightarrow f} \right]_{f \rightarrow c} + (1 - C_s) \alpha, \quad (5)$$

where C_s is a user-fixed coefficient set to 0.5 for this study. The subscripts $c \rightarrow f$ and $f \rightarrow c$ denote interpolating from cell centers to face centers and vice versa. Raeini *et al.*⁴⁵ showed that the use of the smoothed α field for the curvature calculation is efficient in reducing spurious currents in microfluidic two-phase flow problems. In Appendix B, we present a comparison of the local flow dynamics between interFoam and interGCFoam under identical mesh resolution and Courant number. The results emphasize the necessity of using interGCFoam for accurate flow field characterization.

C. Numerical implementation

We mostly used the interFoam solver from OpenFOAM V8³⁹ to resolve the governing equations [Eqs. (1)–(3)]. The NS Eqs. (1) and (2) were solved using the pressure implicit with splitting of the operator (PISO) discretization method, developed by Issa *et al.*⁴⁶ To improve the simulation accuracy, the temporal, spatial gradients, and divergence terms were discretized based on the Euler, central difference, and second-order van Leer scheme,^{39,40} respectively. The multi-dimensional limiter for explicit solution (MULES) algorithm⁴² was used to solve the transport Eq. (3) for the phase field. For all the

TABLE II. List of main mesh-independence test results for 2D and 3D simulations. Here, error refers to the relative bubble length difference with the consecutive mesh.

2D mesh	Cell size (μm)	Bubble length (μm)	Error	3D mesh	Cell size (μm)	Bubble length (μm)	Error
1	4	196	5.6%	1	6	185	14%
2	1.1	207	1%	2	2	215	0%
3	1	209	...	3	1.5	215	...

simulations reported here, the residuals for α , p , and \vec{U} fields were set at 10^{-8} , 10^{-7} , and 10^{-6} , respectively. To resolve the simulation results accurately close to the interfaces, we sometimes used interGCFoam solver from GeochemFoam 5.0⁴⁰ to solve the governing Eqs. (1)–(3). These results are presented in Sec. IV B.

1. Initial and boundary conditions

We implemented appropriate initial and boundary conditions (BCs) implemented in the numerical setup to mimic the experimental conditions. As illustrated in Fig. 1, at time $t = 0$ s, the water phase and CO_2 fill the main and bottom channels, respectively. Under the isothermal assumption made, only pressure and velocity conditions were applied. The water inlet velocity was fixed at 0.0833 m s^{-1} following the experiments of Ho *et al.*¹¹ The inlet velocity of CO_2 was not measured experimentally since CO_2 pressure was controlled upstream before the microfluidic inlet, and we used it as our fitting parameter to assess and match the experimental value of the emulsion/bubble length. At the inlets, no pressure gradient was imposed. As listed in Table I, a uniform pressure value was applied to the outlet, ranging from 0.25 to 9.5 MPa, depending on the case considered. Zero gradients of velocity and phase field (α) were imposed at the outlet. The common no-slip boundary condition was applied to the stationary walls for the velocity field.⁴⁷ Regarding the pressure boundary conditions, we used the fixedFluxPressure and zeroGradient BCs with the interFoam and interGCFoam solvers, respectively.⁴⁸ The former sets the pressure gradient to a specific value such that the (mass) flux at the boundary matches the velocity BC at the walls.⁴⁹ The latter sets the normal gradient of pressure ($\frac{\partial p}{\partial n}$ in the direction normal to the wall), at the boundary to zero⁵⁰ and has been found to yield more stable numerical results with the interGCFoam solvers. The contact angle, θ , is modeled through the static contact angle model, where we assume a purely hydrophilic condition as observed experimentally.¹¹ Therefore, is fixed at 0 to the walls for all cases considered.

2. Mesh independence

We discretized the computational domain using uniform hexahedral mesh grids to minimize the numerical errors. We performed 2D and 3D simulations for ten different flow conditions. Mesh-independence tests were performed for the lowest Ca case using three different mesh sizes listed in Table II. A solution was considered mesh-independent when the variation in bubble length, L_b , between two grid settings was below 5%. As a result, mesh resolutions of $1.1 \mu\text{m}/\text{cell}$ and $2 \mu\text{m}/\text{cell}$ were sufficient for 2D and 3D simulations, respectively, to achieve an accurate estimation of L_b with interFoam.

As discussed previously, numerical artifacts can be present for low Ca in interFoam. Hence, we further investigated the dependency of 3D simulations on mesh resolution using interGCFoam. The

velocity magnitude $|\vec{U}|$ profiles along the middle line of selected planes, normalized by the maximum velocity, U_{\max} , are illustrated in Fig. 2 for three mesh resolutions: 2, 1.5, and $1.4 \mu\text{m}/\text{cell}$. The spatial positions of the selected planes and middle lines are also depicted on the bubble inserted into the plots. As seen in Fig. 2(b), the mesh resolution of $2 \mu\text{m}/\text{cell}$ predicts well the velocity variation along the chosen lines, but adjacent to the interface, the normalized velocity values vary compared to the finer mesh resolutions. Therefore, for our analysis of the internal flow dynamic given in Sec. IV B, we selected a finer mesh resolution of $1.5 \mu\text{m}/\text{cell}$ to ensure mesh independence near the interface.

The time independence study was conducted by varying the Courant number (Co). Our results indicate that a $\text{Co} = 0.25$, corresponding to a time step of 2.3×10^{-7} in 2D and 1.65×10^{-7} in 3D, is sufficient to ensure time independence in our simulations. The

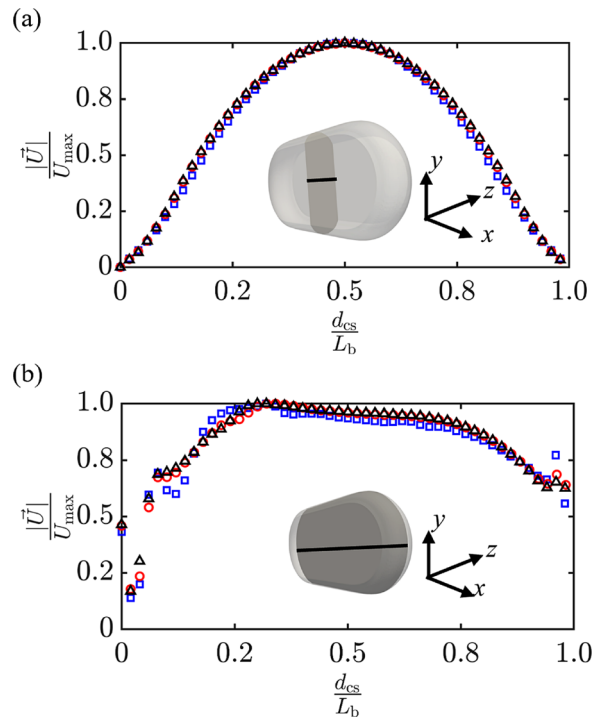


FIG. 2. Variation of normalized velocity profile along the middle line d_{CS} on the cross section of (a) X-normal and (b) Z-normal planes. The symbols of \triangle , \circ , and \square represent mesh sizes of 1.4 , 1.5 , and $2 \mu\text{m}/\text{cell}$, respectively, demonstrating that a mesh size of $1.5 \mu\text{m}/\text{cell}$ is sufficient to ensure flow field mesh independence within the emulsion.

Courant number (Co) was set to $\text{Co} \leq 0.25$ as also prescribed in the literature for such flows^{33,51}. Here, the Co of each cell is defined as⁵²

$$\text{Co} = \frac{\Delta t}{2V} \sum_{j=1}^{N_f} |\phi_j|, \quad (6)$$

where Δt and V are each mesh cell's local time step and volume, respectively. The term $\phi_j = \vec{U} \cdot \vec{S}_f$ is the flux passing through face j with the surface normal vector of $\vec{S}_f = S_f \vec{n}_f$. Here, S_f is the surface area of face j , and N_f is the number of faces for each cell, which is six for hexahedral meshes. The simulation time step was taken as the minimum of all local time steps.

III. VALIDATION

We selected several numerical problems from existing literature to benchmark our numerical model. We discuss 3D simulation results in this section, with two additional 2D cases presented in Appendix A.

A. 3D flow of air bubbles dispersed in water

We examined the motion of air bubbles in water flowing through a T-junction with a width of $120\ \mu\text{m}$, a scenario previously simulated by Santos and Kawaji²⁹ using commercial software (ANSYS Fluent, V6.2). Employing the VOF model, the authors showed that their simulation results were mesh-independent at a resolution of $5.67\ \mu\text{m}/\text{cell}$ using hexahedral mesh grids. We used a slightly finer mesh of $3.5\ \mu\text{m}/\text{cell}$ to ensure a more accurate simulation, with the fluid properties given in Table III. The static contact angle model is employed with a fixed value of 36° , and the surface tension between air and water is set at $0.0735\ \text{N}/\text{m}$.²⁹

Figure 3(a) illustrates the instantaneous volume fraction contours of air bubbles moving in continuous water flow in a microchannel based on our simulations, compared with a similar contour obtained by Santos and Kawaji in Fig. 3(b). The variation of the ultimate bubble length (L_b) with the inlet velocity of water (U_c) is shown in Fig. 3(c), compared to the numerical and experimental results of Santos and Kawaji.²⁹ Although our simulations overpredict the bubble length for $U_c \leq 0.1\ \text{ms}^{-1}$, our predictions align more closely with the experimental findings than those of Santos and Kawaji.²⁹ For higher flow rates where $U_c > 0.1\ \text{ms}^{-1}$, our numerical results are in good agreement with the experimental values.

B. 3D flow of hexanediol emulsions dispersed in poly(vinyl alcohol)

The second benchmark problem concerns the experimental work of Van der Graaf *et al.*⁵³ and the numerical study of Boruah *et al.*⁵⁴ on

TABLE III. Main thermophysical properties of the fluids used for the 3D benchmark problems. Benchmark 1 is the simulation of air bubbles in water. Benchmark 2 is the simulation of hexanediol emulsions in poly(vinyl alcohol). Here, ρ and μ refer to the density and dynamic viscosity of the particular phase, respectively.

Phase	ρ (kg m^{-3})	μ (Pa s)
Air (dispersed)	1.204	1.8×10^{-5}
Water (continuous)	998.2	10^{-3}
1,6-hexanediol diacrylate (dispersed)	1000	1.95×10^{-3}
2 wt. % poly(vinyl alcohol) (continuous)	1020	6.71×10^{-3}

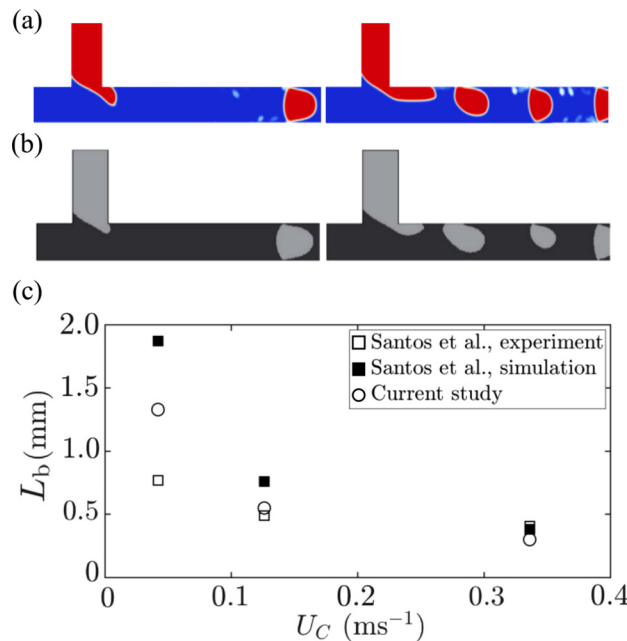


FIG. 3. Volume fraction contours of air bubbles dispersed in water flowing through a microfluidic T-junction on the middle plane of the channel, resulting from (a) current and (b) Santos and Kawaji²⁹ simulations. (c) Variation of the ultimate bubble length (L_b) with the average inlet velocity of the continuous phase (U_c) from the current work compared to results from Santos and Kawaji.²⁹ Reproduced with permission from Santos and Kawaji, Int. J. Multiphase Flow 36, 314 (2010). Copyright 2009 Elsevier Ltd.

hexanediol emulsions flowing in a continuous flow of poly(vinyl alcohol), in a T-junction with a channel width $W = 100\ \mu\text{m}$. In the numerical study by Boruah *et al.*,⁵⁴ a mesh resolution of $7\ \mu\text{m}/\text{cell}$ led to a solution independent of the mesh size. Hence, we used a similar mesh size. The fluid properties used are listed in Table III. The static contact angle model is employed with a fixed value of 0 degrees, and the surface tension between hexanediol and poly(vinyl alcohol) is set at $0.005\ \text{N}/\text{m}$.

An instantaneous snapshot of the α field at the middle plane of the channel from our work is illustrated in Fig. 4(a) for a continuous phase flow rate of $Q_c = 2\ \text{ml}/\text{h}$ and the dispersed phase flow rate of $Q_d = 0.2\ \text{ml}/\text{h}$. A snapshot from the experiments of Van der Graaf *et al.*⁵³ and simulation results of Boruah *et al.*⁵⁴ under similar flow conditions are also illustrated in Figs. 4(b) and 4(c) for comparison. Our results closely match the numerical results for the emulsion growth and detachment processes. When compared to the experiments, the emulsion size just detached and moving downstream in the main channel is slightly overpredicted. This result is also evident in Fig. 4(d), where the variation of L_b with Q_c from our work is illustrated in comparison to the available literature. Nevertheless, for $Q_c \geq 2\ \text{ml}/\text{h}$, our simulation results coincide with both the numerical and experimental findings.

In summary, various benchmark cases in this section and the Appendix show consistent agreement between our simulation results and others, validating and verifying our numerical model to accurately capture bubble and emulsion dynamics in microchannels.

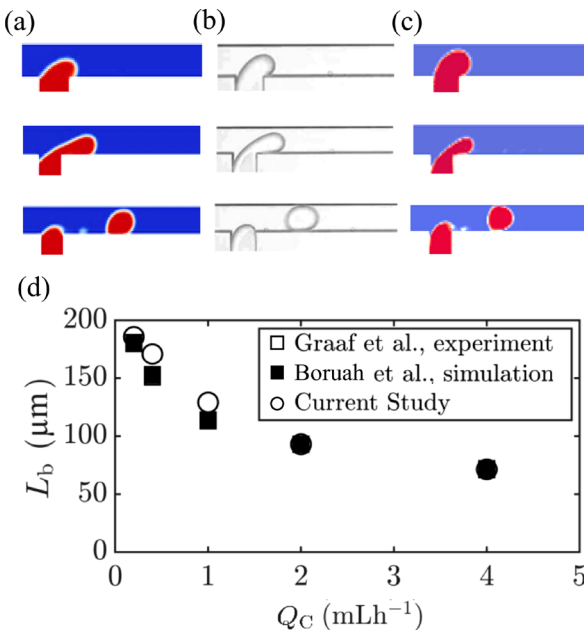


FIG. 4. Volume fraction contours of poly emulsion dispersed in hexanediol flowing through a microfluidic T-junction, projected on the middle plane of the channel, resulting from (a) current simulation, (b) experiments by Van der Graaf *et al.*,⁵³ and (c) Boruah *et al.*⁵⁴ simulations. The snapshots are not to scale. (d) Variation of the bubble length, L_b , with the volumetric flow rate of the continuous phase, Q_C , compared to the literature. Reproduced with permission from Boruah *et al.*, Phys. Fluids **30**, 122106 (2018). Copyright 2018 AIP Publishing.

IV. RESULTS AND DISCUSSION

In this section, the emulsion/bubble lengths obtained from 2D and 3D numerical simulations are compared to their experimental counterparts. Subsequently, we investigate the detailed flow dynamics of a downstream 3D immiscible CO_2 emulsion/bubble in a gaseous (1.45 MPa, $\text{Ca} = 3 \times 10^{-3}$), liquid (8.5 MPa, $\text{Ca} = 6.5 \times 10^{-3}$), and SC (9.5 MPa, $\text{Ca} = 5.7 \times 10^{-3}$) state.

A. Comparison of emulsion/bubble length

We performed 2D and 3D simulations using our validated numerical model with fluid properties given in Table I. Given the immiscibility assumption in our current study, we did not simulate or capture the mass transfer between the phases. The initial experimental emulsion/bubble length of $212 (\pm 7) \mu\text{m}$ was used as the simulations' validation value. For low outlet pressures of 0.25 and 1.45 MPa, CO_2 is in a gaseous state, and as shown in Fig. 5, the emulsion/bubble lengths from 2D and 3D simulations closely follow the experimental value of $212 \mu\text{m}$. As the pressure increases to values over 3.45 MPa and especially after the CO_2 changes from gaseous to liquid or SC state, 2D simulations significantly underpredict the emulsion length compared to the experimental values. In contrast, 3D simulations predict well the emulsion/bubble length for the different outlet pressures and maintain an almost constant threshold of $\approx \pm 5\%$ around the experimental length. In the Taylor flow regime, the emulsion/bubble length increases with the inlet velocity of the dispersed phase, as observed

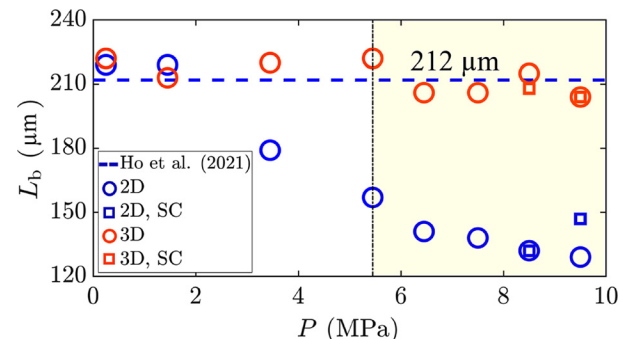


FIG. 5. CO_2 emulsion/bubble length (L_b) varied with outlet pressure (P) resulting from 2D (blue \circ , \square) and 3D simulations (red \circ , \square). Experimental value of $L_b = 212 \mu\text{m}$ from Ho *et al.*¹¹ is also shown with a dashed line for reference. Here, SC refers to the supercritical state of CO_2 . The highlighted area indicates the liquid and supercritical region.

experimentally by Garstecki *et al.*¹⁵ Both our 2D and 3D results are consistent with this trend.

In our study, increasing the inlet velocity of CO_2 in 2D simulations to match with the experimental data led to a stratified flow regime instead. This results prompted us to lower the CO_2 inlet velocity to the maximum at which emulsion/bubble production still occurred. Conversely, in 3D simulations, higher inlet velocities of CO_2 still facilitated Taylor emulsion/bubble production. During Taylor emulsion/bubble production, the dispersed phase enters the main channel and gradually obstructs it. As this obstruction builds, it restricts the flow of the continuous phase passing through the main channel, leading to an increase in pressure in the upstream region of the obstruction. Once the pressure is sufficiently large to overcome the surface tension force of the dispersed phase, the interface is squeezed and pinched off to form a Taylor emulsion/bubble.^{15,55}

As our flow regime is defined with $\text{Ca} < 0.01$, surface tension plays a key role. Initially, surface tension resists emulsion/bubble detachment. However, at the pinch-off moment, it favors detachment, forming emulsions/bubbles to minimize surface energy. Our 2D simulations fail to predict the correct emulsion/bubble production as the surface tension coefficient reduces, revealing limitations due to the curvature estimation based on one dimension. This highlights the challenge of 2D simulations in capturing the 3D complexities of surface tension effects and emulsion/bubble dynamics in rectangular microchannels, consistent with the observations of Mehta *et al.*⁵⁶

In brief, our findings reveal the necessity of 3D simulations to accurately capture two-phase flow in low-aspect-ratio microchannels with a small width. Figure 5 illustrates the significant difference between 2D and 3D results, with the latter more accurately predicting Taylor emulsion/bubble behaviors. Consequently, we used comprehensive 3D simulations to further explore CO_2 emulsion/bubble flow behavior across gaseous, liquid, and supercritical states.

B. 3D dynamics of internal flow

We continued the simulations until the size of the generated emulsions/bubbles stabilized, changing by no more than 5% downstream of the main channel. For these established emulsions/bubbles, we defined a pseudo-Lagrangian reference frame centered on the

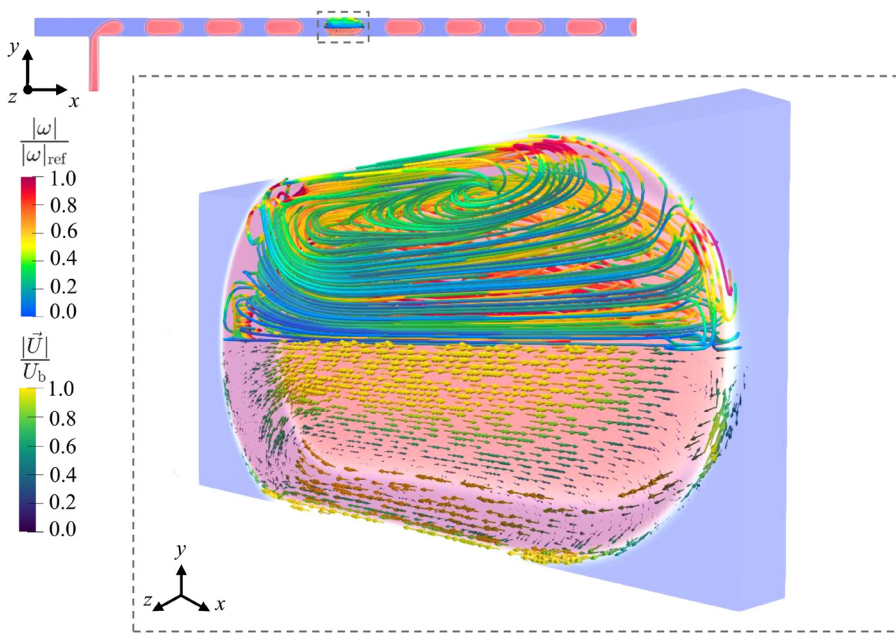


FIG. 6. 3D flow field within a SC CO₂ emulsion (shaded in red; $\alpha = 0$) with the surrounding water (shaded in light blue; $\alpha = 1$) at $P = 9.5$ MPa observed in a moving reference frame at the emulsion's volume-averaged velocity (U_b). Inside the emulsion, the top half shows the streamlines colored by the normalized vorticity and the bottom half demonstrates the velocity vectors colored by the normalized velocity magnitude. Here, U_b represents the emulsion's mean velocity, while $|\omega|_{\text{ref}}$ denotes the reference vorticity magnitude, set at $50\,000\text{ s}^{-1}$.

emulsion/bubble's centroid by subtracting the emulsion/bubble's volume-averaged velocity (U_b) from the global velocity field. The simulation data were obtained using interGCFoam solver (GeochemFoam, v5.0) and post-processed with the open-source software ParaView (V5.11).

Figures 6 and 7 (Multimedia view) present the internal flow dynamics of a SC CO₂ emulsion at the outlet pressure of $P = 9.5$ MPa and $\text{Ca} = 5.7 \times 10^{-3}$. In Fig. 6, the top half displays 3D streamlines colored by the vorticity magnitude, $|\omega|$, normalized by $|\omega|_{\text{ref}} = 50\,000\text{ s}^{-1}$,

$$\vec{\omega} = \left(\frac{\partial U_z}{\partial y} - \frac{\partial U_y}{\partial z} \right) \vec{i} + \left(\frac{\partial U_x}{\partial z} - \frac{\partial U_z}{\partial x} \right) \vec{j} + \left(\frac{\partial U_y}{\partial x} - \frac{\partial U_x}{\partial y} \right) \vec{k}. \quad (7)$$

The bottom half illustrates the velocity vectors in the chosen pseudo-Lagrangian reference, colored by the resultant velocity magnitude, $|\vec{U}|$, normalized by U_b . Here, only a small fraction of velocity vectors are shown for better visibility. This comprehensive visualization helps characterize the flow field and vortex patterns within the emulsion, with vorticity magnitude shedding light on vortex intensity. Meanwhile, the velocity vector field offers insights into flow orientation and local flow accelerations, pinpointing areas with energetic flow in the emulsion. Figure 7 (Multimedia view), with an increased number of streamlines, illustrates the detailed rotational structures in the emulsion, orthogonal to the main flow direction.

Figures 6 and 7 (Multimedia view) illustrate the complex internal flow within CO₂ emulsion/bubble, highlighting predominant

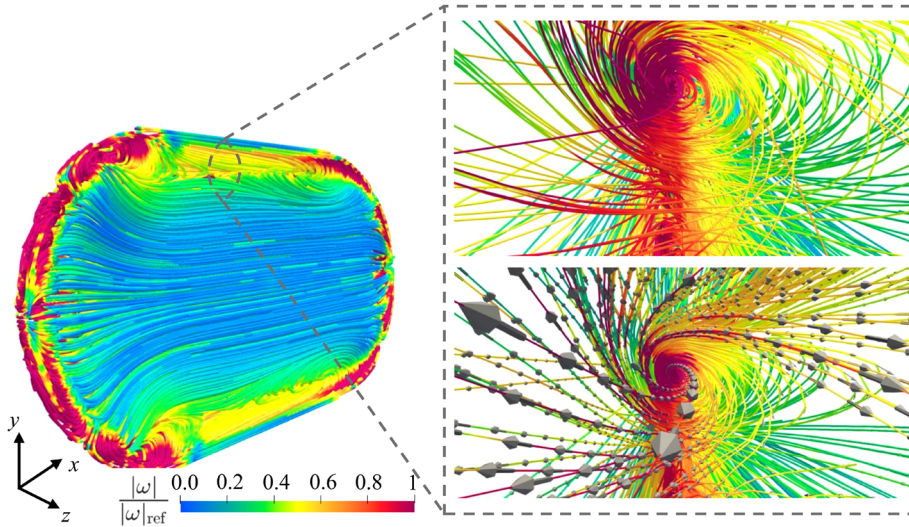


FIG. 7. 3D flow field within a SC CO₂ emulsion at $P = 9.5$ MPa, observed in a moving reference frame at the emulsion's volume-averaged velocity (U_b). The streamlines are colored by the normalized vorticity magnitude. Zoomed-in view of the orthogonal vortex structure existing within the emulsion. The gray velocity vectors indicate the direction of rotation. Multimedia available online.

circulation patterns around the z and y axis, respectively. The immiscible interface between the emulsion/bubble and the surrounding phase prevents mixing between the two phases,^{2,57} leading to recirculation patterns and non-uniform flow field. This circulating and non-uniform flow arises from the drag exerted by the faster surrounding water flow on the interfacial region of the slower-moving CO₂ emulsion/bubble.

The 3D streamlines are intertwined and can curve in all three dimensions. Higher vorticity regions are observed close to the emulsion/bubble interface, especially near the sidewalls. The 3D velocity vectors reveal CO₂ acceleration in the emulsion/bubble's central area, aligned with the main streamwise flow direction. Notably, within the emulsion/bubble's depth, velocity vectors indicate fluid motion across the z -direction, particularly near the emulsion/bubble caps. These observations indicate the intricate 3D internal dynamics of CO₂, characterized by rotational structures and areas of flow acceleration and deceleration.

In Fig. 7 (Multimedia view), the complexity of the flow dynamics is further emphasized by the presence of organized rotational structures. These patterns, characterized by high vorticity magnitudes, reveal a coherent flow path aligned with the velocity vector field,

depicted by gray vectors. These structures are predominantly located near the interfacial regions, indicating their significance for potential mixing and exchange processes. This observation highlights the areas of interest crucial for advancing our understanding of transport phenomena utilizing Taylor emulsions/bubbles.

To elucidate the intricate 3D flow structures within the emulsions/bubbles, we examined the flow patterns through various slices in both the streamwise (x) and lateral (z) directions. This method involves projecting the 3D flow field onto these planes, displaying the velocity field accordingly. The vorticity ($\vec{\omega}$) presented corresponds to the magnitude of 3D vorticity [Eq. (7)] on the selected planes.

1. 3D flow fields projected on streamwise x-y planes

For our analysis, we selected three x - y planes at $z/W = 0.2, 0.5$, and 0.9 . Figure 8 presents the projected velocity vectors in the lower half, with corresponding 2D streamlines in the top half of each panel. Columns represent the gaseous, liquid, and SC states, providing comprehensive flow dynamics for each phase. The liquid and SC emulsions show nearly identical flow patterns on these slices. Our results agree

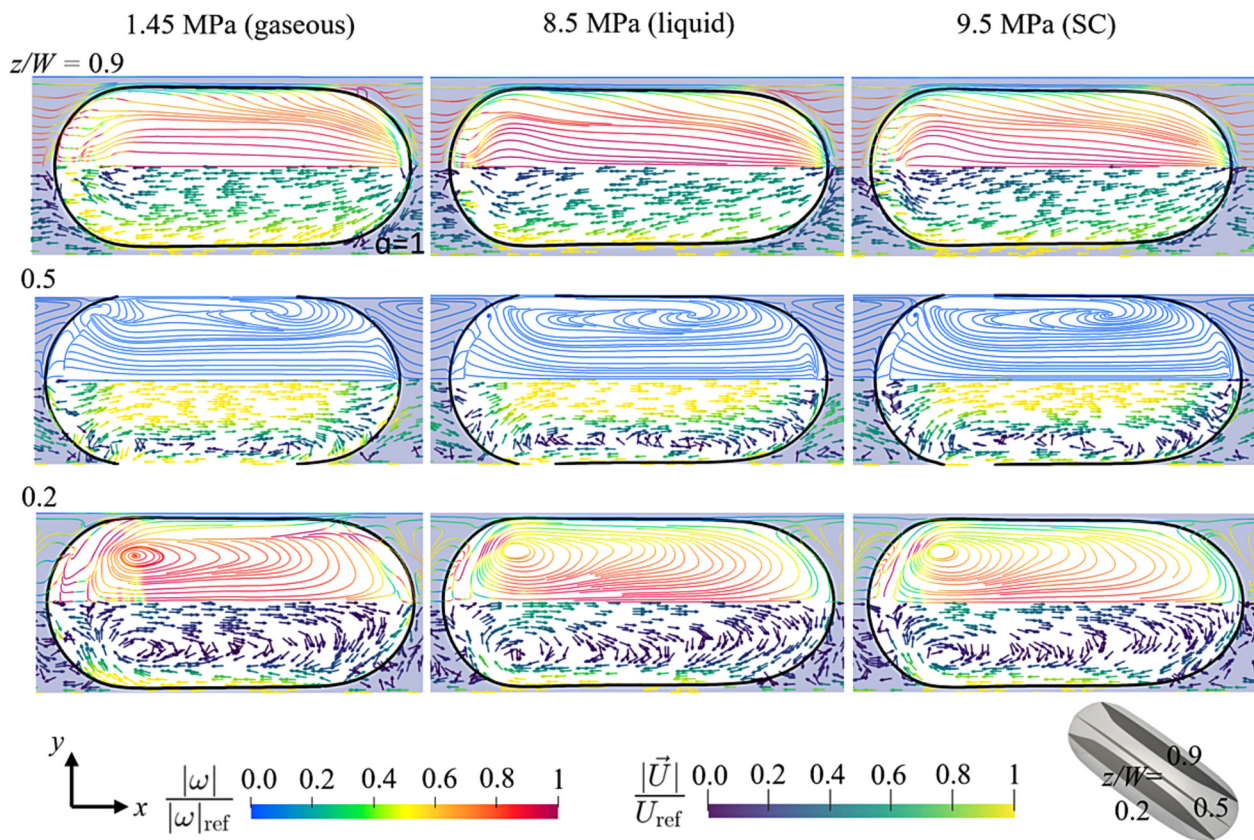


FIG. 8. CO₂-in-water emulsion/bubble flow behavior (observed in a moving reference frame at velocity, U_b) on three different planes and outlet pressures. The planes are parallel to the x - y plane and normal to the z -direction. The CFD results are obtained using interGCFoam. The top half of the panels show the streamlines colored by the normalized vorticity magnitude, and the bottom half demonstrate the velocity vectors colored by the normalized velocity magnitude. The emulsion/bubble interface is marked by a thick black curve on each panel. The surrounding water area is shaded in light blue, distinguishing it from the interior of the bubble/emulsion. Here, U_{ref} and $|\omega|_{\text{ref}}$ are fixed at 0.2 m/s and 50 000 s⁻¹.

with the μ -PIV findings of Liu *et al.*²⁶ who reported similar flow patterns in x - y planes for $3.2 \times 10^{-3} \leq Ca \leq 3.8 \times 10^{-2}$.

At $z/W = 0.9$, all CO_2 emulsions/bubbles at different phases exhibit backward flow (in $-\hat{x}$ direction) as observed in the moving reference frame at U_b . Adjacent to the sidewall (at $z/W = 0.9$), the fluid layers within the emulsions/bubbles are dragged toward the rear of the emulsion/bubble due to sidewall drag forces. For all the phases, the streamlines show high vorticity magnitude [of $O(10^5) \text{ s}^{-1}$] throughout, accompanied by moderate velocity magnitude. The velocity magnitude is particularly high at the interface regions of the emulsion/bubble's body and rear cap, which accelerates the flow in these areas. Despite significant projected vorticity on this plane, no distinct vortex or flow patterns develop. This is attributed to the proximity to the sidewalls where the flow within each emulsion/bubble predominantly follows the motion imposed by the sidewalls.

Across all scenarios at $z/W = 0.5$, the highest velocities are observed in the middle part of the plane, characteristic of the Poiseuille flow. This observation is consistent with the micro-particle image velocimetry (μ -PIV) visualizations by Oishi *et al.*²³ The gaseous state shows a distinct increase in velocity at the caps, likely due to the surrounding flow that can easily accelerate the bubble flow due to the lower density and reduced inertia of gaseous CO_2 . Another explanation is due to the presence of numerical artifacts. Spurious currents have been shown to be particularly present for lower dispersed phase density.⁵⁸ However, the use of interGCFoam, which effectively limits the development of nonphysical velocity at the interface, ensures that such effects are minimized.⁴⁰

At $z/W = 0.5$, a pair of elongated recirculation occurs for all cases, with circulation motion close to the top and bottom walls. The top and bottom walls drag the fluid layers inside the emulsion/bubble through the thin film. The closed shape of the emulsion/bubble and the immiscibility between the phases induce the recirculation patterns inside the emulsions/bubbles. The liquid and SC states exhibit a clear elongated vortex pair, slightly different from the gaseous state's vortex pattern, which shows a wavier circulation and slight differences in the flow field direction near the cap regions. At the rear and front cap regions, a slight shift in the velocity vectors' orientation occurs to follow the motion of the surrounding water flow due to the shear stress exerted by the surrounding water. The gaseous state, with a dynamic viscosity three to four times lower than the SC and liquid states, shows dynamics influenced by the surrounding flow region. Furthermore, at $z/W = 0.5$, the vorticity magnitude is rather low, indicating the limited capacity of the vortex patterns to enhance mixing. This plane is characterized by translational motion at the center and minor vortex flow close to the top and bottom walls.

Closer to the sidewalls, i.e., $z/W = 0.2$, the circulation patterns differ from those observed at $z/W = 0.5$. Across the cases, we observe larger vortex patterns with enhanced vorticity magnitude, which are indicative of enhanced circulation. However, the velocity magnitude is lower on the plan of $Z/W = 0.2$ compared to the case of $z/W = 0.5$. Hence, the top and bottom walls, moving at the emulsion/bubble velocity, drag fluids in an extent area at $z/W = 0.2$, leading to a large circulation pattern compared to the case of $z/W = 0.5$. CO_2 exhibits more recirculation motion close to the rear cap region.

Our 3D simulation results reveal complex flow patterns with spatially non-uniform vorticities in CO_2 emulsions/bubbles, particularly intense vortical structures rotating along the \hat{x} axis close to the

emulsion/bubble interfaces. In addition, distinct flow patterns are dominant at different depths; enhanced rotational strength beneficial for mixing is observed on the plane of $z/W = 0.2$, whereas mostly translational motion is noted for the middle plane at $z/W = 0.5$. 2D CFD models would not be able to capture such unique vortex patterns and, hence, are inadequate to obtain comprehensive and accurate local flow fields.

2. 3D flow fields projected on spanwise y - z planes

We analyzed the flow on three slices parallel to the y - z plane at $x/L_b = 0.2, 0.5$, and 0.9 , shown in Fig. 9, for the three CO_2 states investigated. The top half of each panel presents the streamlines colored by the normalized projected vorticity magnitude from Eq. (7), and the bottom half shows the velocity vector field colored by the normalized velocity magnitude.

At $x/L_b = 0.9$, in the downstream region, the liquid and supercritical (SC) states of CO_2 emulsion display no noticeable vortices. This contrasts with the gaseous state, where two small counter-rotating vortices with elevated vorticity magnitude are visible, highlighting the significant influence of drag from the surrounding flow and its ability to alter the flow for CO_2 bubbles. These vortices are characterized by high vorticity magnitude, indicating profound recirculation patterns in this region. The velocity magnitude is notably higher at the tips of the CO_2 bubble where the vortices are present. In the gaseous state, the flow remains at the bubble's front (top) tip and recirculates energetically, whereas in the liquid and SC states, the flow is redirected toward the emulsion's body.

Liquid and SC CO_2 flow at $x/L_b = 0.5$ display almost identical flow patterns with one pair of moderate-sized vortices and one pair of small-sized vortices (at the emulsion tip). The moderate-sized vortices display enhanced vorticity magnitude and may present higher potential for exchange mechanism within the emulsion. These vortices are especially visible in Fig. 7 (Multimedia view) and are generated by the combined wall drag actions, following the fluid continuity within the curved emulsion boundary.

At $x/L_b = 0.2$, near the emulsion's rear cap region, the liquid and SC states present larger vortices within the emulsion body next to the sidewalls. Those vortices are located farther into the emulsion body due to the presence of larger circulation motions induced by the top and bottom walls in this region compared to the case of $x/L_b = 0.5$. Concerning the gaseous state, the strong vortices stay located close to the top and bottom interfaces due to the predominant influence of the surrounding flow.

3. Quantifying Q-criterion

To further analyze and better understand the vortex patterns depicted previously, we used a 3D method of vortical structure identification based on the Q-criterion (Q_{cr}). Unlike methods relying solely on vorticity magnitude, the Q-criterion enables the distinction of vortical structures and curved streamlines by effectively filtering out the irrotational parts of the flow, which may exhibit elevated vorticity magnitudes.^{51,59,60} Q_{cr} is defined as⁵⁹

$$Q_{\text{cr}} = \frac{1}{2} (|\mathbf{W}|^2 - |\mathbf{D}|^2), \quad (8)$$

where $\mathbf{W} = \frac{1}{2} [\nabla \mathbf{U} - (\nabla \mathbf{U})^T]$ is the anti-symmetric part of the velocity gradient tensor representing the local rotation part, and

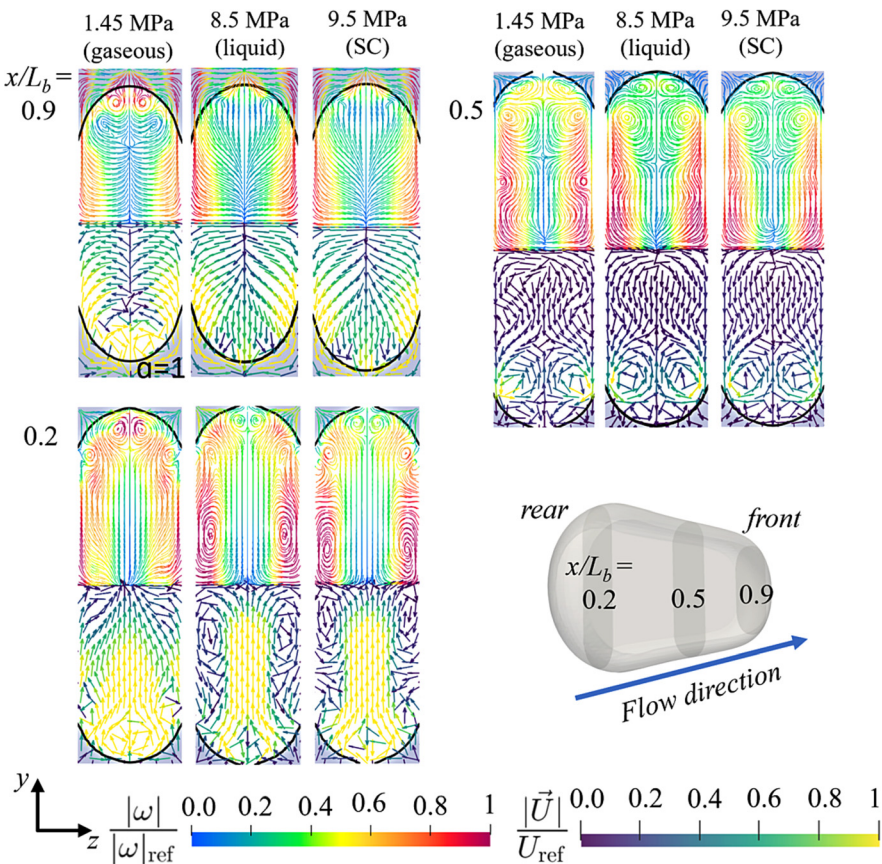


FIG. 9. Flow behavior on three different y - z planes within a CO_2 emulsion/bubble at different pressures. The planes are parallel to the y - z plane and normal to the x -direction, at $x/L_b = 0.2, 0.5$, and 0.9 . The top half of the emulsions/bubbles shows the streamlines colored by the normalized vorticity magnitude, and the bottom half demonstrates the velocity vectors colored by the normalized velocity magnitude. The emulsion/bubble interface is marked by a thick black curve on each panel. The surrounding water area is shaped in light blue, distinguishing it from the interior of the bubble/emulsion. Here, U_{ref} and $|\omega|_{\text{ref}}$ are fixed at 0.05 m/s and 50000 s^{-1} , respectively.

$\mathbf{D} = \frac{1}{2}[\nabla \mathbf{U} + (\nabla \mathbf{U})^T]$. \mathbf{D} is the symmetric strain tensor, representing local deformation rate. Physically, the Q-criterion identifies zones where locally the flow rotates at a rate higher compared to its deformation, occurring whenever $Q_{\text{cr}} > 0$. According to this definition, only the strongest rotational patterns that surpass the deformation strength subsist.⁶¹ We normalize it as follows: $Q_{\text{cr},n} = Q_{\text{cr}}/10^9$. Figure 10 illustrates isosurfaces of two selected $Q_{\text{cr},n}$ thresholds for the three thermodynamic states investigated, colored with normalized vorticity magnitude.

From the left side of Fig. 10, the inner regions of the emulsions/bubbles with $Q_{\text{cr},n} > 0.005$ demonstrate that numerous strong vortical structures are present within the emulsions/bubbles and predominantly dominate over strain for all cases observed. Adjacent to the sidewalls, the patterns are characterized by higher vorticity magnitude, consistent with the observations in Figs. 8 and 9. Overall, the gaseous state exhibits more patterns and higher vorticity magnitudes, with some areas, such as the front cap region, appearing cluttered. Conversely, the liquid and SC states exhibit vortical patterns of lower vorticity magnitude that are more uniformly distributed throughout the emulsion body. This suggests the higher potential of the gaseous bubble to enhance circulatory motion compared to the liquid and SC phases.

The right column of Fig. 10 displays flow regions with relatively stronger rotation patterns with $Q_{\text{cr},n} > 0.05$. These patterns are all colored in high vorticity magnitude, emphasizing their rotational

strength. In the gaseous state, most of these patterns aggregate close to the bubble body interface and cap regions, as also observed in Fig. 9. This suggests a tendency for lower Ca bubbles to favor circulation at the interfacial region.

In the liquid and SC emulsions, we see dominant loci adjacent to their rear, where multiple vortices coexist, consistent with the orthogonal vortice patterns across the z -direction in Fig. 9 at $x/L_b = 0.2$. Interestingly, an enhanced rotational structure near the tip of the emulsion is also noticeable, which was not captured by the selected slices. This indicates that the surrounding flow of water can influence liquid and SC emulsions, though the effect remains localized at the extreme tip. These observations suggest that the vortex patterns in the third dimension (i.e., the orthogonal streamwise direction vortices) represent some of the strongest existing rotational structures and may be of significant interest for enhancing exchange and mixing phenomena.

V. CONCLUSIONS

In this study, we have conducted a detailed examination of the dynamics of Taylor flow in gaseous, liquid, and supercritical CO_2 states in a microfluidic channel. Through comprehensive computational fluid dynamics (CFD) simulations, using 2D and 3D models and corroborating with experimental data, our research highlights the crucial role of 3D modeling to accurately capture the complex flow behaviors associated with these systems.

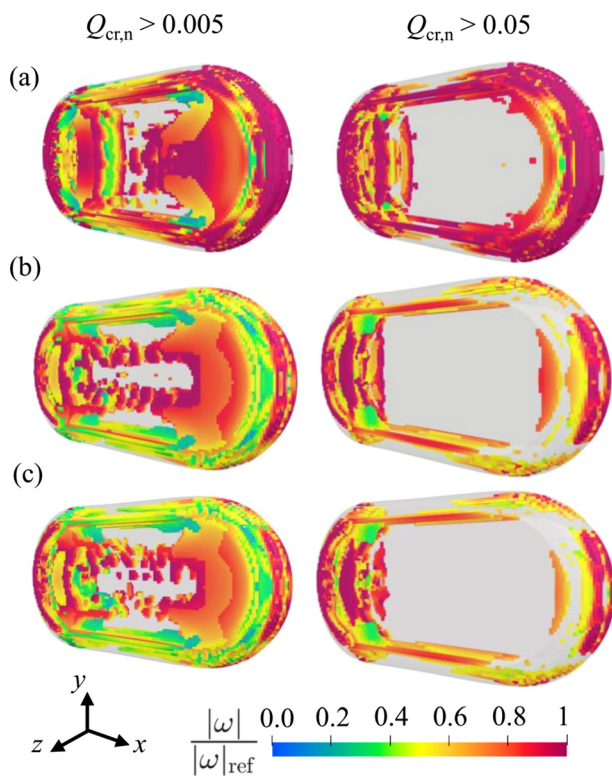


FIG. 10. Q-criterion normalized based on isosurfaces of the emulsion/bubble's internal flow for the (a) gaseous, (b) liquid, and (c) SC CO₂. Here, the surfaces are colored by the vorticity magnitude, normalized by $|\omega|_{\text{ref}} = 50\,000 \text{ s}^{-1}$.

Our findings show the necessity of utilizing 3D numerical models, particularly for liquid and SC CO₂ cases, where two-dimensional simulations are inadequate. The 3D simulations, conducted using interGCFoam, reveal intricate internal flow dynamics in the emulsions/bubbles that are not observable with simpler 2D models. The 3D simulations are crucial in identifying vortex patterns along both streamwise and spanwise dimensions, which exhibit intense rotational motions essential for understanding solute transport and mixing behaviors.

Our analysis reveals that bubbles with lower capillary numbers, such as the gaseous state CO₂, tend to form intense rotational patterns close to the body interface of the bubble. In contrast, higher capillary number emulsions, representative of liquid and SC states, develop significant rotational patterns predominantly in the upstream region of the flow. These patterns, elucidated by our Q-criterion analysis, indicate complex vorticity fields that are critical for the effective design and operation of microfluidic devices across various applications, including chemical analysis and material synthesis. Furthermore, the examination of spanwise planes revealed larger vortex patterns with higher vorticity magnitude closer to the sidewalls, a phenomenon often overlooked in previous studies.

Our study complements 3D experimental investigations, which often face challenges in accurately capturing the third dimension of flow and vorticity fields due to curved emulsion/bubble interfaces. It also provides a quantitative understanding of internal flow hydrodynamics. Overall, our advanced 3D simulations provide a clearer and more

comprehensive understanding of Taylor flow dynamics, affirming the complex interplay between hydrodynamic forces and capillary effects. These findings are crucial for refining current models and enhancing the predictive capabilities of simulations in microfluidic applications.

In future investigations, we emphasize the necessity of employing advanced 3D simulations to thoroughly examine the thin film area, particularly around CO₂ bubbles. The current challenge lies in accurately capturing the thin film using the algebraic volume of fluid (VOF) method, which diffuses the interface across 2–3 cells. An alternative method, the piecewise linear interface calculation (PLIC) method,⁶² could potentially enhance interface accuracy. However, implementing this method requires careful consideration to avoid spurious currents and to minimize increases in computational time. Additionally, adopting a dynamic rather than a static contact angle could offer a more realistic depiction of scenarios. Finally, a critical gap in both our study and existing literature is a systematic examination of how the aspect ratio influences the flow fields within the emulsion and the surrounding fluid.

ACKNOWLEDGMENTS

We gratefully acknowledge the support from the Canada First Research Excellence Fund (CFREF), Future Energy Systems (FES T02-P05 CCUS projects) at the University of Alberta, and Canada Foundation for Innovation (CFI 34546). P. A. T. holds a Canada Research Chair (CRC) in Fluids and Interfaces and gratefully acknowledges funding from the Natural Sciences and Engineering Research Council of Canada (NSERC) and Alberta Innovates (AI), particularly through the NSERC Canada Research Chairs Program (CRC 233147) and Discovery Grant (RGPIN-2020-05511), as well as AI Advance (202102818).

AUTHOR DECLARATIONS

Conflict of Interest

The authors have no conflicts to disclose.

Author Contributions

Santhosh Virappane: Conceptualization (supporting); Data curation (lead); Formal analysis (equal); Investigation (lead); Methodology (equal); Software (lead); Validation (equal); Visualization (equal); Writing – original draft (equal); Writing – review & editing (equal).

Reza Azadi: Formal analysis (equal); Visualization (equal); Writing – review & editing (supporting). **Neelarun Mukherjee:** Investigation (supporting); Software (supporting). **Peichun Amy Tsai:** Conceptualization (lead); Formal analysis (equal); Funding acquisition (lead); Investigation (equal); Resources (lead); Supervision (lead); Validation (equal); Visualization (equal); Writing – review & editing (lead).

DATA AVAILABILITY

The data that support the findings of this study are available from the corresponding author upon reasonable request.

APPENDIX A: 2D BENCHMARK SIMULATIONS

Two 2D benchmark flow scenarios from the literature are also investigated: (1) water emulsions in air and (2) oil emulsions in

TABLE IV. Main fluid properties used for the 2D simulations of the benchmark scenarios. Here, benchmark 1 comprises the flow of water emulsions in the air, and benchmark 2 simulates the flow of water emulsions in oil.

Fluid	Phase	Density (kg m^{-3})	Viscosity ($\text{m}^2 \text{s}^{-1}$)
Water	Dispersed	998	1.002×10^{-6}
Air	Continuous	1.2	6.6667×10^{-3}
Water	Dispersed	1000	0.001
Oil	Continuous	900	0.02

water. The numerical setups, the flow properties utilized, and the corresponding results are also provided here for reference.

1. 2D water emulsions dispersed in air

We used the 2D case of Malekzadeh and Roohi⁶³ to investigate the dispersed water motion in a flow of air. The dimensions of the T-junction in their study was $L \approx 4 \text{ mm}$, and in our case, the length is 3 mm. We also utilized the same mesh settings and fluid properties listed in Table IV. Here, the surface tension is fixed at 0.0728. Malekzadeh and Roohi⁶³ investigated different contact angles and flow rates at two fixed $\text{Ca} = 0.006$ and $\text{Ca} = 0.036$. Figures 11(a) and 11(b) illustrate volume fraction contours obtained from our 2D simulations for $\text{Ca} = 0.006$ and $\text{Ca} = 0.036$, respectively. Each panel shows emulsion formation stages from filling to breaking up at different time steps (t_1, t_2, t_3, t_4 , and t_5). Our results are in good agreement with the reference.⁶³

The time periods required for each emulsion formation stage, from filling to breakup, are estimated and illustrated in Fig. 12 for three different contact angles, θ , compared to the results from Malekzadeh and Roohi⁶³ and for two Ca values. Overall, our results

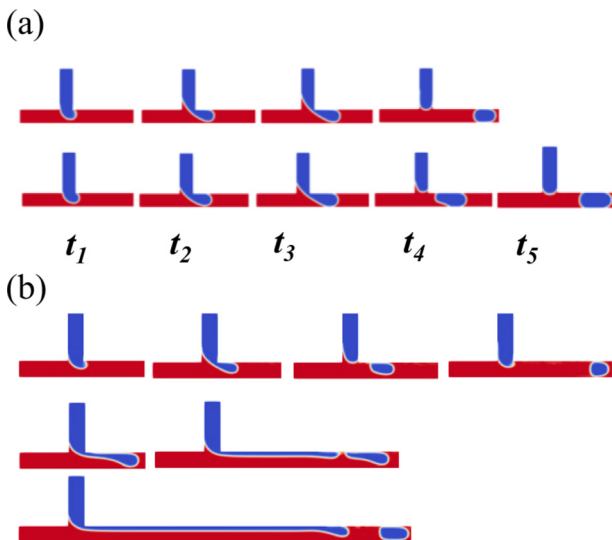


FIG. 11. Volume fraction contours of the dispersed phase, projected on the middle plane of the channel, resulting from simulations of $\text{Ca} = 0.006$ (a) and $\text{Ca} = 0.036$ (b). Each panel illustrates the sequence of the emulsion formation stages, including filling (t_1, t_2), blocking (t_3), pinching-off (t_4), and breakup (t_5).

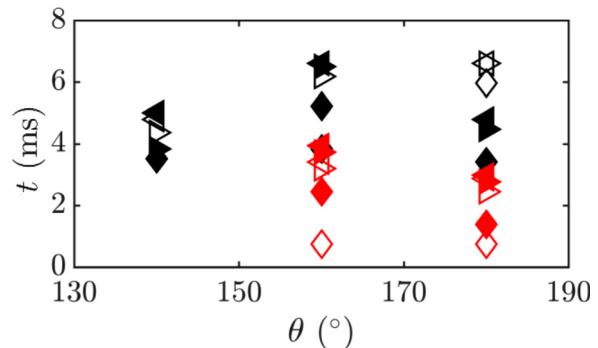


FIG. 12. Time periods of different emulsion formation stages, including blocking (\blacklozenge), pinching-off (\blacktriangleright), and breakup (\blacktriangleleft) for different contact angles, θ . Here, $t = 0 \text{ s}$ corresponds to the filling stage. The results from the current simulations are highlighted by filled symbols, and those from Malekzadeh and Roohi⁶³ with empty symbols. Moreover, black and red colored symbols correspond to $\text{Ca} = 0.006$ and $\text{Ca} = 0.036$, respectively.

follow those from Ref. 63, especially at low Ca ($\text{Ca} = 0.006$). In that case, the only noticeable deviation is for larger θ values where the blocking stage occurs relatively faster, but there is somewhat a compensatory effect in our simulations with the time required for the emulsions to break up being relatively longer.

2. 2D water emulsions dispersed in oil

Here, we investigated the dispersed motion of water emulsions in oil flow from the study of Singh⁶⁴ and varied the surface tension value, σ , to examine its impact on the resultant emulsion length, L_b . The fluid properties utilized are listed in Table V. The contact angle was assumed to be $\theta = 135^\circ$ for all tested cases.

Singh⁶⁴ used the level-set method using commercial software (Comsol, v5.3) with triangular mesh grids. For this problem, we conducted a mesh independence study to ensure that our solutions are not affected by the quadrilateral uniform mesh size we use. The interFoam solver of an open-source code (OpenFOAM, v8) was used to track the two-phase flow and solve the NS equations. Table V lists the difference between the estimated emulsion lengths for three mesh sizes. Our results show that a mesh with $\approx 10\,000$ cells was sufficient for a mesh-independent solution.

The variation of L_b with σ , estimated from our simulations, is shown in Fig. 13 compared to the results of Singh.⁶⁴ For $\sigma \leq 40 \text{ mNm}^{-1}$, our results show an almost linear increase in L_b with σ , in excellent agreement with the results of Singh.⁶⁴

TABLE V. Resultant emulsion length and relative difference for three sizes of 2D mesh cells for mesh independence test. Here, error refers to the relative bubble length difference with the consecutive mesh.

Number of cells	Emulsion length (μm)	Error %
5 201	68.8	9.5
10 542	76.1	1.3
14 925	76	...

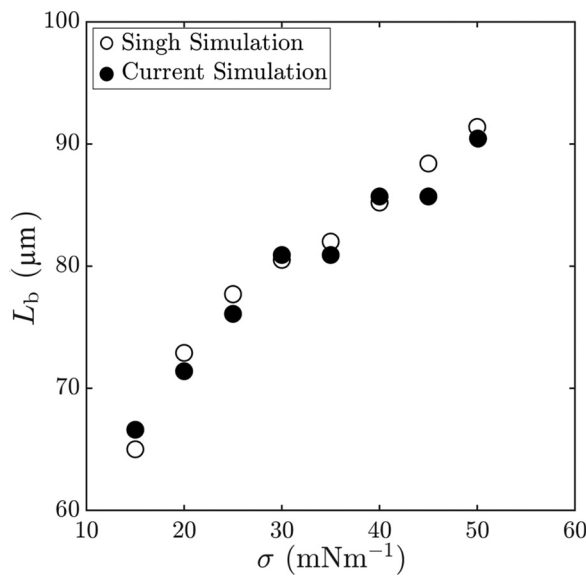


FIG. 13. Variation of the emulsion length, L_b , with the interfacial tension between oil and water, σ , in the current simulations compared to those of Singh.⁶⁴

APPENDIX B: COMPARISON BETWEEN INTERFOAM AND INTERGCFOMA RESULTS

In Fig. 14, we compare numerical results obtained using interFoam in (a) and interGCFoam in (b), showing the velocity magnitude (U_{mag}) projected on the XY middle for a specific 3D case (1.45 MPa), under identical mesh and Courant number conditions. Both solvers adequately capture the bubble's shape and size. However, there are significant differences in their local flow fields. The results from interFoam in (a) show spurious velocities as high

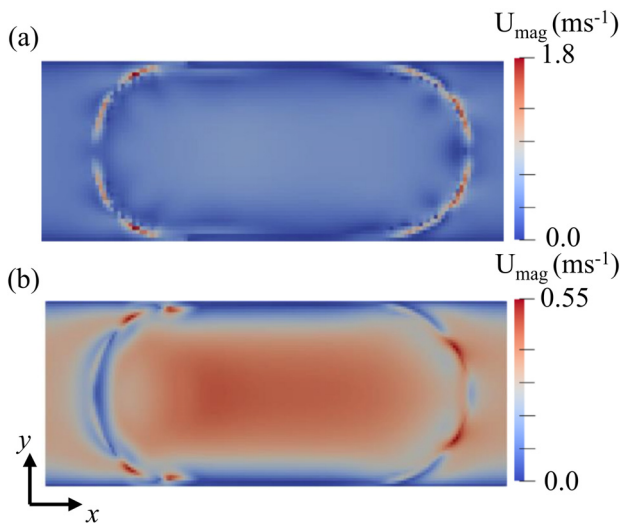


FIG. 14. Comparison of the numerical results of the projected velocity magnitude on the XY middle plane between using (a) interFoam and (b) interGCFoam solver.

as 1.8 m/s near the interface, far exceeding typical speeds observed in the microchannel. In contrast, the interGCFoam solver provides more physically accurate results, with velocities peaking at 0.55 m/s, within the suitable range observed in the emulsions/bubbles. This comparison highlights the reliability and superior accuracy of interGCFoam in simulating local flow field dynamics, such as streamlines, vorticity, and velocity fields, in CO₂ Taylor emulsions/bubbles.

REFERENCES

- ¹C. Holtze, "Large-scale droplet production in microfluidic devices—An industrial perspective," *J. Phys. D: Appl. Phys.* **46**, 114008 (2013).
- ²C. Yao, Y. Zhao, H. Ma, Y. Liu, Q. Zhao, and G. Chen, "Two-phase flow and mass transfer in microchannels: A review from local mechanism to global models," *Chem. Eng. Sci.* **229**, 116017 (2021).
- ³K. S. Elvira, X. C. I Solvas, R. C. Wootton, and A. J. Demello, "The past, present and potential for microfluidic reactor technology in chemical synthesis," *Nat. Chem.* **5**, 905 (2013).
- ⁴R. Riahi, A. Tamayol, S. A. M. Shaegh, A. M. Ghaemmaghami, M. R. Dokmeci, and A. Khademhosseini, "Microfluidics for advanced drug delivery systems," *Curr. Opin. Chem. Eng.* **7**, 101 (2015).
- ⁵L. Nan, H. Zhang, D. A. Weitz, and H. C. Shum, "Development and future of droplet microfluidics," *Lab Chip* **24**, 1135 (2024).
- ⁶C. Kleinstreuer, J. Li, and J. Koo, "Microfluidics of nano-drug delivery," *Int. J. Heat Mass Transfer* **51**, 5590 (2008).
- ⁷R. Juanes, E. Spiteri, F. Orr, and M. Blunt, "Impact of relative permeability hysteresis on geological CO₂ storage," *Water Resour. Res.* **42**, W12418, <https://doi.org/10.1029/2005WR004806> (2006).
- ⁸H. E. Huppert and J. A. Neufeld, "The fluid mechanics of carbon dioxide sequestration," *Annu. Rev. Fluid Mech.* **46**, 255 (2014).
- ⁹Y. Cohen and D. H. Rothman, "Mechanisms for mechanical trapping of geologically sequestered carbon dioxide," *Proc. Math. Phys. Eng. Sci.* **471**, 20140853 (2015).
- ¹⁰Y. Sun, Q. Li, D. Yang, and X. Liu, "Laboratory core flooding experimental systems for CO₂ geosequestration: An updated review over the past decade," *J. Rock Mech. Geotech. Eng.* **8**, 113 (2016).
- ¹¹T.-H. M. Ho, J. Yang, and P. A. Tsai, "Microfluidic mass transfer of CO₂ at elevated pressures: Implications for carbon storage in deep saline aquifers," *Lab Chip* **21**, 3942 (2021).
- ¹²S. S. Datta, I. Battiatto, M. A. Fernø, R. Juanes, S. Parsa, V. Prigobbe, E. Santanach-Carreras, W. Song, S. L. Biswal, and D. Sinton, "Lab on a chip for a low-carbon future," *Lab Chip* **23**, 1358 (2023).
- ¹³A. Bordbar, A. Taassob, A. Zarnaghsh, and R. Kamali, "Slug flow in microchannels: Numerical simulation and applications," *J. Ind. Eng. Chem.* **62**, 26 (2018).
- ¹⁴V. Talimi, Y. Muzychka, and S. Kocabiyik, "A review on numerical studies of slug flow hydrodynamics and heat transfer in microtubes and microchannels," *Int. J. Multiphase Flow* **39**, 88 (2012).
- ¹⁵P. Garstecki, M. J. Fuerstman, H. A. Stone, and G. M. Whitesides, "Formation of droplets and bubbles in a microfluidic T-junction—Scaling and mechanism of break-up," *Lab Chip* **6**, 437 (2006).
- ¹⁶R. K. Shah, H. C. Shum, A. C. Rowat, D. Lee, J. J. Agresti, A. S. Utada, L.-Y. Chu, J.-W. Kim, A. Fernandez-Nieves, C. J. Martinez *et al.*, "Designer emulsions using microfluidics," *Mater. Today* **11**, 18 (2008).
- ¹⁷A. V. Kovalev, A. A. Yagodnitsyna, and A. V. Bilsky, "Flow hydrodynamics of immiscible liquids with low viscosity ratio in a rectangular microchannel with T-junction," *Chem. Eng. J.* **352**, 120 (2018).
- ¹⁸Y. Zhao, G. Chen, and Q. Yuan, "Liquid-liquid two-phase flow patterns in a rectangular microchannel," *AIChE J.* **52**, 4052 (2006).
- ¹⁹A. Etmiran, Y. S. Muzychka, and K. Pope, "A review on the hydrodynamics of Taylor flow in microchannels: Experimental and computational studies," *Processes* **9**, 870 (2021).
- ²⁰U. Mießner, T. Helmers, R. Lindken, and J. Westerweel, " μ PIV measurement of the 3D velocity distribution of Taylor droplets moving in a square horizontal channel," *Exp. Fluids* **61**, 125 (2020).

- ²¹X. Chao, F. Xu, C. Yao, T. Liu, and G. Chen, "CFD simulation of internal flow and mixing within droplets in a T-junction microchannel," *Ind. Eng. Chem. Res.* **60**, 6038 (2021).
- ²²S. Jakiela, S. Makulskia, P. M. Korczyk, and P. Garstecki, "Speed of flow of individual droplets in microfluidic channels as a function of the capillary number, volume of droplets and contrast of viscosities," *Lab Chip* **11**, 3603 (2011).
- ²³M. Oishi, H. Kinoshita, T. Fujii, and M. Oshima, "Simultaneous measurement of internal and surrounding flows of a moving droplet using multicolour confocal micro-particle image velocimetry (micro-PIV)," *Meas. Sci. Technol.* **22**, 105401 (2011).
- ²⁴S. Ma, J. M. Sherwood, W. T. Huck, and S. Balabani, "On the flow topology inside droplets moving in rectangular microchannels," *Lab Chip* **14**, 3611 (2014).
- ²⁵R. Azadi, J. Wong, and D. S. Nobes, "Determination of fluid flow adjacent to a gas/liquid interface using particle tracking velocimetry (PTV) and a high-quality tessellation approach," *Exp. Fluids* **62**, 48 (2021).
- ²⁶Z. Liu, L. Zhang, Y. Pang, X. Wang, and M. Li, "Micro-PIV investigation of the internal flow transitions inside droplets traveling in a rectangular microchannel," *Microfluid. Nanofluid.* **21**(12), 180 (2019).
- ²⁷C. D. Meinhart, S. T. Wereley, and J. G. Santiago, "PIV measurements of a microchannel flow," *Exp. Fluids* **27**, 414 (1999).
- ²⁸F. Guo and B. Chen, "Numerical study on Taylor bubble formation in a micro-channel T-junction using VOF method," *Microgravity Sci. Technol.* **21**, 51 (2009).
- ²⁹R. M. Santos and M. Kawaji, "Numerical modeling and experimental investigation of gas-liquid slug formation in a microchannel T-junction," *Int. J. Multiphase Flow* **36**, 314 (2010).
- ³⁰S. M. Mousavi and B. J. Lee, "Investigation of bubble structure in a microchannel under microgravity conditions: Effects of discontinuous wettability with dynamic contact angle," *Acta Astronaut.* **201**, 394 (2022).
- ³¹A. Bordbar, S. Kheirandish, A. Taassob, R. Kamali, and A. Ebrahimi, "High-viscosity liquid mixing in a slug-flow micromixer: A numerical study," *J. Flow Chem.* **10**, 449 (2020).
- ³²S. Vivekanand and V. Raju, "Numerical study of the hydrodynamics and heat transfer characteristics of liquid-liquid Taylor flow in microchannel," *Heat Transfer—Asian Res.* **47**, 794 (2018).
- ³³A. E. M. Mora, A. L. F. de Lima e Silva, and S. M. M. de Lima e Silva, "Numerical study of the dynamics of a droplet in a T-junction microchannel using OpenFOAM," *Chem. Eng. Sci.* **196**, 514 (2019).
- ³⁴C. Falconi, C. Lehrenfeld, H. Marschall, C. Meyer, R. Abiev, D. Bothe, A. Reusken, M. Schlüter, and M. Wörner, "Numerical and experimental analysis of local flow phenomena in laminar Taylor flow in a square mini-channel," *Phys. Fluids* **28**, 012109 (2016).
- ³⁵G. Y. Soh, G. H. Yeoh, and V. Timchenko, "Numerical investigation on the velocity fields during droplet formation in a microfluidic T-junction," *Chem. Eng. Sci.* **139**, 99 (2016).
- ³⁶D. M. Weekes, D. A. Salvatore, A. Reyes, A. Huang, and C. P. Berlinguet, "Electrolytic CO₂ reduction in a flow cell," *Acc. Chem. Res.* **51**, 910 (2018).
- ³⁷R. Masel, Z. Liu, D. Zhao, Q. Chen, D. Lutz, and L. Nereng, "CO₂ conversion to chemicals with emphasis on using renewable energy/resources to drive the conversion," in *RSC Green Chemistry* (Royal Society of Chemistry, 2016), Vol. 2016, pp. 215–257.
- ³⁸Z. Xu, Y. Wang, Y. Chen, M. H. Spalding, and L. Dong, "Microfluidic chip for automated screening of carbon dioxide conditions for microalgal cell growth," *Biomicrofluidics* **11**, 064104 (2017).
- ³⁹C. J. Greenshields *et al.*, *OpenFOAM User Guide, Version 3* (OpenFOAM Found. Ltd, 2015), p. 47.
- ⁴⁰J. Maes and H. P. Menke, "Geochemfoam: Direct modelling of multiphase reactive transport in real pore geometries with equilibrium reactions," *Transp. Porous Media* **139**, 271 (2021).
- ⁴¹J. U. Brackbill, D. B. Kothe, and C. Zemach, "A continuum method for modeling surface tension," *J. Comput. Phys.* **100**, 335 (1992).
- ⁴²H. Rusche, Ph.D. thesis (Imperial College London, University of London, 2003).
- ⁴³D. A. Hoang, V. van Steijn, L. M. Portela, M. T. Kreutzer, and C. R. Kleijn, "Benchmark numerical simulations of segmented two-phase flows in micro-channels using the volume of fluid method," *Comput. Fluids* **86**, 28 (2013).
- ⁴⁴C. Galusinski and P. Vigneaux, "On stability condition for bifluid flows with surface tension: Application to microfluidics," *J. Comput. Phys.* **227**, 6140 (2008).
- ⁴⁵A. Q. Raeini, B. Bijeljic, and M. J. Blunt, "Numerical modelling of sub-pore scale events in two-phase flow through porous media," *Transp. Porous Media* **101**, 191 (2014).
- ⁴⁶R. Issa, B. Ahmadi-Befrui, K. Beshay, and A. Gosman, "Solution of the implicitly discretised reacting flow equations by operator-splitting," *J. Comput. Phys.* **93**, 388 (1991).
- ⁴⁷G. K. Batchelor, *An Introduction to Fluid Dynamics* (Cambridge University Press, 2000).
- ⁴⁸OpenCFD Ltd., *OpenFOAM User Guide: Standard Boundary Conditions* (OpenCFD Ltd, 2024).
- ⁴⁹OpenCFD Ltd., *Fixed Flux Pressure* (OpenCFD Ltd, 2023).
- ⁵⁰OpenCFD Ltd., *General—Zero Gradient Condition* (OpenCFD Ltd, 2017).
- ⁵¹R. Azadi and D. S. Nobes, "Local flow dynamics in the motion of slug bubbles in a flowing mini square channel," *Int. J. Heat Mass Transfer* **178**, 121588 (2021).
- ⁵²R. Azadi and D. S. Nobes, "On the three-dimensional features of a confined slug bubble in a flowing square capillary," *Phys. Fluids* **33**, 033327 (2021).
- ⁵³S. Van der Graaf, T. Nisisako, C. Schroën, R. Van Der Sman, and R. Boom, "Lattice Boltzmann simulations of droplet formation in a t-shaped microchannel," *Langmuir* **22**, 4144 (2006).
- ⁵⁴M. P. Boruah, A. Sarker, P. R. Randive, S. Pati, and S. Chakraborty, "Wettability-mediated dynamics of two-phase flow in microfluidic T-junction," *Phys. Fluids* **30**, 122106 (2018).
- ⁵⁵M. De Menech, P. Garstecki, F. Jousse, and H. A. Stone, "Transition from squeezing to dripping in a microfluidic t-shaped junction," *J. Fluid Mech.* **595**, 141 (2008).
- ⁵⁶H. B. Mehta, J. Banerjee, M. P. Bambhaniya, and J. B. Desai, "CFD analysis on Taylor slug flow through 3D vertical mini-channel," in *International Conference on Microchannels* (ASME, 2011), Vol. 44649, pp. 309–315.
- ⁵⁷C. N. Baroud, F. Gallaire, and R. Dangla, "Dynamics of microfluidic droplets," *Lab Chip* **10**, 2032 (2010).
- ⁵⁸A. Q. Raeini, M. J. Blunt, and B. Bijeljic, "Modelling two-phase flow in porous media at the pore scale using the volume-of-fluid method," *J. Comput. Phys.* **231**, 5653 (2012).
- ⁵⁹J. C. Hunt, A. A. Wray, and P. Moin, "Eddies, streams, and convergence zones in turbulent flows, Studying turbulence using numerical simulation databases, 2," in *Proceedings of the 1988 Summer Program* (1988).
- ⁶⁰M. Roth, *Automatic Extraction of Vortex Core Lines* (ETH Zurich, 2000), Vol. 9.
- ⁶¹Y.-n Zhang, X.-y Wang, Y.-n Zhang, and C. Liu, "Comparisons and analyses of vortex identification between omega method and q criterion," *J. Hydron. Dyn.* **31**, 224 (2019).
- ⁶²V. R. Gopala and B. G. Van Wachem, "Volume of fluid methods for immiscible-fluid and free-surface flows," *Chem. Eng. J.* **141**, 204 (2008).
- ⁶³S. Malekzadeh and E. Roohi, "Investigation of different droplet formation regimes in a T-junction microchannel using the VOF technique in OpenFOAM," *Microgravity Sci. Technol.* **27**, 231 (2015).
- ⁶⁴A. Singh, "Effect of interfacial tension on droplet generation in T-junction microfluidic device," in *Proceedings of the COMSOL Conference in Bangalore* (2018).